CrystEngComm

Accepted Manuscript

ROYAL SOCIETY OF CHEMISTRY

www.rsc.org/crystengcomm

Influence of Fluorine Side-Group Substitution on the Crystal Structure Formation of Benzene-1,3,5-trisamides

Christoph Zehe,[a] Marko Schmidt,[a] Renée Siegel,[a] Klaus Kreger,[b] Venita Daebel,[c] Sandra Ganzleben,[b] Hans-Werner Schmidt[b] and Jürgen Senker*[a]

[a] Inorganic Chemistry III and Bayreuth Center for Colloids and Interfaces, University of Bayreuth, 95447, Bayreuth, Germany; E-mail: juergen.senker@uni-bayreuth.de; Tel: (+49) 921-55-2788;

[b] Macromolecular Chemistry I, Bayreuth Institute of Macromolecular Research and Bayreuth Center for Colloids and Interfaces, University of Bayreuth, 95447, Bayreuth, Germany

[c] Bruker Biospin GmbH, Silberstreifen 4, 76287 Rheinstetten, Germany

Abstract

By a combination of powder X-ray diffraction, multidimensional and multinuclear solid-state NMR spectroscopy as well as quantum chemical calculations, we were able to determine the crystal structure of 1,3,5-tris(2-fluoro-2-methylpropionylamino)benzene. Solid-state NMR experiments guided the structure solution by predicting the content of the asymmetric unit and the presence of a NH---OC hydrogen bond network. In addition to a real space structure solution and a Rietveld refinement, quantitative symmetry-based $^{19}F^{19}F$ double-quantum recoupling experiments provided a cost function to determine the positions of the methyl groups and fluorine atoms. The structure solution of this particular fluorine-substituted trisamide illustrates the impact of fluorine side-group substitution on the common columnar packing motif of benzene-1,3,5-tricarboxamides. In the case of 1,3,5-tris(2,2-dimethylpropionylamino)benzene, the supramolecular aggregation is then guided by the formation of triple helical NH---OC hydrogen bond networks within the individual columns. In contrast, the substitution of one methyl group by a fluorine atom in each side chain results in a two-dimensional NH---OC hydrogen bond pattern leading to a lamellar crystal structure with only van der Waals interactions between the layers. Since fluorine is not involved in the hydrogen bond network and both chemical units exhibit a similar steric demand the fundamental structural differences are most probably caused by changes of the molecular polarity.

Introduction

The ability of reversibly forming complex supramolecular structures and polymers by secondary intermolecular interactions like hydrogen bonding, aromatic π-π stacking or electrostatic and dispersion interactions between the constituting parts lead to the field of supramolecular chemistry.[1,2] *Via* the concept of molecular recognition, the targeted synthesis and design of molecules allows to tune the strength and direction of the secondary intermolecular interactions.[2] For instance, adjusting the number and direction of intermolecular interactions leads to columnar,[3–5] layer-like[6] or three-dimensionally propagating hydrogen bond networks.[7]

In particular, the class of benzene-1,3,5-tricarboxamides (BTAs) has evolved into an attractive supramolecular motif in recent years.[8] Through cooperative hydrogen bonding in a helical pattern one-dimensional columnar aggregates which exhibit large dipole moments are formed.[4,5,9,10,11] The antiparallel arrangement of such macrodipoles leads to a fast one-dimensional growth resulting in columnar supramolecular structures.[12,13] The easy chemical accessibility and tuneability renders BTAs into a versatile class of advanced materials with increasing importance in many fields of research.[8] For instance, they show potential as organogelators,[7,14] hydrogelators,[15] liquid crystals,[16] MRI contrast reagents,[17] and metal complexation reagents.[18] In addition, some derivatives are known to be highly efficient electret, clarifying and nucleating agents for semi-crystalline polymers, e.g. isotactic polypropylene,[19] polybutylene terephthalate,[20] poly-(ethylene-co-propylene),[21] polyvinylidene fluoride[22] or polylactides.[23]

The structure solution of BTA compounds, however, is often difficult since only microcrystalline powders are available, rendering single crystal X-ray diffraction experiments impossible. Due to the coincidence of symmetry-equivalent reflexes and the heavy overlap of higher order reflexes,[24] structure solutions based on *ab initio* powder X-ray diffraction (PXRD) are often hampered. Topological information such as unit cell constants and global arrangements of molecules might still be obtained with reasonable accuracy, but local structural details are usually strongly affected.[24,25] Here, solid-state nuclear magnetic resonance (NMR) spectroscopy offers complementary information: based on the three basic interactions - chemical shift,[26] dipolar interaction[27] and quadrupolar splitting[28] - local structural properties may be extracted and combined with PXRD data at different steps of the structure solution.[29]

Symmetry information such as the content of the asymmetric unit can be obtained through Wyckoff spectra,[30] high resolution experiments or by direct determination of symmetry

elements through exploiting orientational correlations of chemical shift tensors.[24,31] Hetero- and homonuclear dipole interactions may be used to extract distances, torsion angles as well as to select correct space groups and to verify structure models, respectively.[13,25,32,33,34] This combination of X-ray diffraction experiments and solid-state NMR spectroscopy – often called NMR crystallography- has proven to be a powerful tool for structure elucidation, being capable of tackling problems which are unsolvable by any of these methods alone.[6,13,25,33,34,35] A more thorough discussion of the topic NMR-crystallography including an overview over the recent literature may be found in ref. 36.

In order to understand the structure directing interactions, the bulk structures of several BTA derivatives were examined in the past by PXRD.[3,9,13,37,38] Here, sterically less demanding side groups as e.g methyl groups prefer two- or three-dimensional hydrogen bond networks.[7,37] In contrast, bulky moieties as *t*-butyl were found to predominantly lead to columnar packing motifs with triple helical hydrogen bonds.[3,9,11,13] Similarly, long linear or only short-branched aliphatic side groups often induce columnar mesophases with an analogous supramolecular organisation pattern at low transition temperatures.[16,39] For such large aliphatic residues, hydrogen bond networks with a two-dimensional topology are observed rarely.[38]

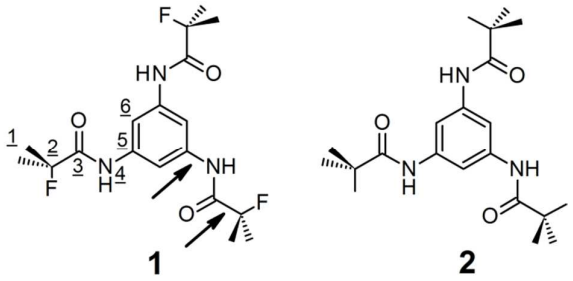

Scheme 1. Left: Molecular structure of 1,3,5-tris(2-fluoro-2-methylpropionylamino)benzene **1** including a labeling scheme for different chemical groups. The black arrows assign the structure directing torsion angles $C_{Ar}C_{Ar}NH$ and NC_OC_QF of the side groups. Right: Molecular structure of 1,3,5-tris(2,2-dimethylpropionylamino)benzene **2**.

In order to investigate the effect of a side-chain substitution with equal sterical demand but different polarity, we synthesized 1,3,5-tris(2,2-dimethylpropionylamino)benzene **1** (Scheme 1). In comparison to the structurally similar 1,3,5-tris(2,2-dimethylpropionylamino)benzene **2**, one methyl group in each side chain is replaced by a fluorine atom. Using a combined approach of PXRD, *ab initio* quantum chemical calculations and solid-state NMR

experiments, we investigate the impact of this fluorine side-group substitution on the packing motif and hydrogen bond pattern.

Experimental

Molecular Characterisation: ^{1}H NMR and ^{13}C NMR solution-state spectra were recorded with a Bruker AC 300 spectrometer (300 and 75 MHz, respectively) at room temperature and referenced to TMS. Mass spectra were recorded on a VARIAN MAT 8500 instrument using direct probe inlet and electron impact ionization. Matrix assisted laser desorption ionization spectrometry with time of flight mass spectrometry (MALDI-TOF MS) measurements were performed on a Bruker Reflex III in reflection mode using trans-2-(3-(4-tert-butylphenyl)-2-methyl-2-propenylidene)malononitrile (DCTB) as matrix. Solutions of the analyte (1 mg/100 µL) and the matrix (1 mg/100 µL) in tetrahydrofuran were mixed in the ratio 5:20 (v:v) and spotted onto the MALDI target plate prior to the measurement. The laser intensity was set to around 20%. Elemental analysis (EA) was performed with a HEKAtech elemental analyzer, EA 3000 (Euro Vector CHNS), charged with tungsten oxide and copper. Detection was performed utilizing a GC setup equipped with a thermal conductivity detector.

Synthesis: All solvents were purified and dried using standard procedures. 2-fluoroisobutyric acid (97%) was purchased from ABCR and used without further purification. 1,3,5-triaminobenzene was freshly synthesized from 3,5-dinitroaniline (obtained from Aldrich and used as received) as described in literature.[13] 2-Fluoroisobutyric acid chloride was synthesized from 2-fluoroisobutyric acid and oxalyl chloride. 2g (18.8 mmol) of 2-fluoroisobutyric acid was dissolved in 30 mL of CH_2Cl_2 (DCM). The mixture was cooled down to 0 °C and after addition of 4.78 g (37.7 mmol) of oxalyl chloride and three drops of DMF it was refluxed overnight. After cooling to room temperature, an excess of potassium stearate was added drop wise (to react excess oxalyl chloride) until no further gas evolution was observed. The 2-fluoroisobutyric acid chloride was then distilled under normal pressure. All resonances in the ^{1}H liquid NMR spectra could be unequivocally assigned to solvents and product. Yield: 1.9 g (15.3 mmol, 81.4 %); ^{1}H-NMR (300 MHz, $CDCl_3$): δ = 1.65 ppm (d, $^{3}J(^{1}H,^{19}F)$ = 20.7 Hz, 6H, -CH_3).

Compound **1** was synthesized by dropping 1.9 g (15.3 mmol) of 2-fluoroisobutyric acid chloride to a mixture of 0.56 g (2.6 mmol) of 1,3,5-triaminobenzene, 15 ml of pyridine and 0.08 of LiCl in 80 mL of THF at 0 °C under argon atmosphere. The reaction was stirred over two days at 70 °C, cooled down to RT and the solvents were evaporated under vacuum. The residual reaction mixture was poured into an excess of water. The precipitate was filtered off,

dried under reduced pressure and recrystallised from methanol. To remove further impurities, the solid was refluxed in 50 mL of n-hexane for three hours, filtered off hot and dried again. Yield: 0.44 g (3.53 mmol, 23 %). ^{1}H-NMR (300 MHz, DMSO-d_6): δ = 1.56 ppm (d, $^{3}J(^{1}H,^{19}F)$ = 21.7 Hz, 6H, -CH_3); 7.75 ppm (s, 3H, Ar-H); 9,94 ppm (d, $^{4}J(^{1}H,^{19}F)$ = 3.2 Hz, 3H, -NH); ^{13}C-NMR (75 MHz, DMSO-d_6): δ = 25.3 ppm (d, $^{2}J(^{13}C,^{19}F)$ = 24 Hz, -CH_3); 95.6 ppm (d, $^{1}J(^{13}C,^{19}F)$ = 182 Hz , -CF); 110.7. ppm (s, -ArH); 138.4. ppm (s, -Ar); 171.3 ppm (d, $^{2}J(^{13}C,^{19}F)$ = 22 Hz , -C=O); MS (70eV), m/z (%): 387 (M+, 100); 344 (22); 326 (47); 299 (17); 69 (8); 61 (31). MALDI-TOF-MS: m/z calcd: 387.18 ($[M]^+$), 410.17 ($[M+Na]^+$), 426.14 ($[M+K]^+$) g/mol, found: 387.05 ($[M]^+$), 410.05 ($[M+Na]^+$), 426.01 ($[M+K]^+$) g/mol; Elemental analysis (N, C, H): calcd 10.8%, 55.8%, 6.2%; found 11.1%, 57.6%, 6.3%.

Solid-State NMR experiments: ^{1}H, ^{13}C and ^{19}F chemical shifts are referenced to TMS and $CFCl_3$, respectively. The ^{15}N chemical shifts are reported relative to nitromethane, where all values are shifted by -380.5 ppm compared to liquid NH_3. All ^{1}H and ^{19}F experiments were performed in a 1.3 mm double resonance probe at a Bruker Avance III HD spectrometer at a field strength of B_0 = 14.1 T. The spin rate for magic angle spinning (MAS) was set to ν_{rot} = 60000 ± 3 Hz for ^{19}F and to ν_{rot} = 65000 ± 3 Hz for ^{1}H. All ^{13}C and ^{15}N experiments were collected with a 4 mm triple resonance probe at a Bruker Avance II spectrometer at a field strength of B_0 = 7.1 T and at a MAS spin rate of ν_{rot} = 12500 ± 1 Hz.

The ^{1}H/^{19}F direct excitation experiments were performed using a nutation frequency of ν_{nut} = 179/150 kHz for the 90° pulse without decoupling of ^{19}F/^{1}H. For the ^{19}F^{19}F double-quantum experiments, a symmetric $R14_4^5$ double-quantum recoupling protocol with the $S_0S_0^{'}\,S_\pi^{'}S_\pi$ supercycle was used.[40] Excitation and reconversion was realised through 90°-270° composite pulses as *R*-elements with a nutation frequency of ν_{nut} = 210 kHz and a maximum excitation time of 2 ms.

The ^{13}C and ^{15}N cross polarisation (CP) spectra were recorded using a ramped lock pulse consisting of 100 intervals with a linear decrease from 50/93 kHz to 25/46.5 kHz on the ^{1}H/^{19}F channel and the power for ^{13}C/^{15}N was experimentally adjusted to the Hartmann-Hahn conditions. The contact time was set to 3 ms for both ^{1}H^{13}C and ^{19}F^{13}C experiments. Due to the high spin density and large gyromagnetic ratio of protons, this time is sufficiently long to allow magnetization transfer from protons to all carbon atoms and hence all carbon atoms will give rise to signals in the ^{1}H^{13}C CP. In contrast, only carbon atoms in spatial proximity to the ^{19}F labels appear in the ^{19}F^{13}C CP, since the used contact time of 3 ms is sufficiently short due to the low spin density of ^{19}F compared to ^{1}H.

Proton broadband decoupling was realised using a SPINAL-64 sequence during acquisition where the nutation frequency and pulse length were set to 65 kHz and 7 µs, respectively. For ^{19}F decoupling a XiX sequence[41] with a pulse length of 7 µs and a nutation frequency of 70 kHz was used.

Solid-State NMR simulations: Simulations of the $^{19}F^{19}F$ DQ build-up curves were performed with the simulation software package SIMPSON.[42] Relative orientations and principal values of the $^{19}F^{19}F$ dipole tensors were calculated based on the possible structure models obtained from PXRD. The asymmetry and anisotropy parameters for the chemical shift anisotropy where estimated from a MAS 1D experiment at ν_{rot} = 3000 ± 2 Hz. The corresponding Euler angles where set to zero for all spins since they seem to show only negligible influence on the supercycled build-up curves,[43] which was tested with different arbitrary angles. For powder averaging 232 (α,β) orientations in combination with 40 γ-angles were used.

In all cases, the experimental curves exhibited lower double-quantum efficiencies than the simulations (see ESI† Figure S1), which might be caused by residual proton couplings.[44] For this reason, all simulated curves were fitted to the experimental ones by applying a constant scaling factor, which was determined as follows: For each structure model, every possible assignment of simulated to experimental curves was taken into account with one individual scaling factor for every set of simulated curves. Each scaling factor was optimised with the software package MATLAB in a least square sense.[45] Subsequently, for every assignment a rms value was calculated in percent according to

$$\mathrm{rms} = 100 \times \sqrt{\frac{\sum_i (\mathrm{exp}_i - \mathrm{sim}_i)^2}{\sum_i (\mathrm{exp}_i)^2}}$$

where exp_i is the experimental and sim_i the simulated data point corresponding to the i^{th} abscissa value. Finally, for each structure model only the assignment with the lowest rms value was considered for the subsequent analysis.

***Ab initio* structure determination using PXRD:** PXRD measurements on compound **1** were carried out on a STOE StadiP diffractometer equipped with a curved germanium monochromator (oriented according to the (111) plane) creating $CuK\alpha_1$ radiation (λ = 1.5406 Å). The samples were filled in a 0.7 mm capillary tube and measured in Debye-Scherrer geometry in the 2Θ range of 2° - 50°. Above 50° hardly any more reflections were observable. The powder patterns were fully handled using REFLEX PLUS from the commercial program

package Accelrys MS Modeling (version 5.0).[46] After indexing, Pawley refinement and assignment of the correct space group, the structure solution step was performed by means of real space methods with the simulated annealing algorithm.[47] For the structure solution the molecule was first geometry optimised with DFT methods (see section Computational Methods). As starting model two molecules were set into the asymmetric unit as one motion group each. Besides the possible translational and rotational degrees of freedom the structure directing torsion angles in each molecule were set free during the structure solution (see Scheme 1, right). Additionally, a preferred orientation correction following the model of March-Dollase was applied during the solution step.[48]

Concerning the Rietveld refinement, at first four cycles, where the atomic parameters were allowed to relax, were carried out using a global isotropic temperature factor for all atoms and a preferred orientation adjustment according to Rietveld-Toraya[49]. The molecular structure was retained without any limitations for the rotational and translational degrees of freedom by taking into account energy considerations through applying the COMPASS forcefield.[50] Nevertheless, the final number of refined structural parameters (see Table 1) is not strictly representative due to the adopted energy constraint. This force field assisted refinement is based on a *combined figure of merit* (R_{comb}) with

$$R_{comb} = (1 - w_{comb}) * wRp + w_{comb} * R_{Energy} \qquad (1)$$

where w_{comb} represents an energy weighting factor that was set to 0.5. The energetic contribution, R_{Energy}, is defined as follows:

$$R_{Energy} = \tanh(0.1 * \frac{E - E_{min}}{E_{tol}}) \qquad (2)$$

where E represents the total energy, E_{min} the energy in the global minimum and E_{tol} an energy window above E_{min} in which possible structure solutions are tolerated. Here, the default value of 40 kcal/mol was used, preventing the break of covalent bonds as well as an overlap of atoms or atom groups during the refinement step, which reduced the real number of refined structural parameters noticeably.

Afterwards, the peak profile including FWHM (pseudo-Voigt) with its profile parameters NA and NB were refined. The pseudo-Voigt peak shape function as a linear combination of a Lorentzian (*L*) and a Gaussian (*G*) includes the Θ-dependent mixing parameter η given by

$$ç(È) = (NA + NB) * 2È \qquad (3)$$

where NA and NB are adjustable parameters. Besides, the lattice parameters, the zero-point shift, sample off-centering, asymmetry correction (Finger-Cox-Jephcoat)[51] and the experimental background using 20 orthogonal polynomials were refined. Relevant crystallographic data are summarized in Table 1. Atomic parameters, the temperature factor and the

occupancy of compound **1** are included in the crystallographic information file being available in the ESI†.

Table 1. Relevant crystallographic data for **1** from PRXD

	1
Formula	$C_{18}H_{24}F_3N_3O_3$
M / g * mol^{-1}	387.38
Crystal system	Monoclinic
Space group	$P2_1$
a / Å	11.886(4)
b / Å	15.395(5)
c / Å	10.554(4)
α / °	90
β / °	95.012(2)
γ / °	90
V / Å^3	1924(2)
Z' / Z	2 / 4
ρ / g * cm^{-3}	1.337
T / K	293
U	0.24(1)
V	-0.033(3)
W	0.0024(2)
NA	0.22(3)
NB	0.005(1)
zero-point shift	0.0061(9)
R_0[(a)]	0.8413
a*	0.142(14)
b*	0.984(2)
c*	0.098(20)
No. ref. struct. par.[(b)]	307
Rp	0.0398
wRp	0.0552

(a) Preferred orientation coefficient of the sample according to the March-Dollase function representing a dimensionless value reflecting the shape of the crystallites; R0 < 1 for platelets, R0 > 1 for needles.

(b) The number of refined structural parameters include one isotropic temperature factor and three translational elements of each atom within the asymmetric unit. Since a COMPASS

force field with an energy constraint was applied, the refinement of the atomic positions is not handled independently.

Creation of additional structure models: In the structure model obtained from PXRD structure solution, the $N_HC_OC_QF$ torsions (see scheme 1) of the two molecules of the asymmetric unit were altered by 60° and 120° in different combinations in order to test the influence on PXRD patterns and $^{19}F^{19}F$ double-quantum build-up curves. During subsequent Rietveld refinement as described above, the structures were allowed to relax. In all cases, $N_HC_OC_QF$ torsion angles of 0° or 120° compared to the original model a) were observed afterwards. Four models were selected for the double-quantum simulations: For model b) one torsion of molecule one changed by 120° (symbolic representation: ↑); for model c) all three torsions of molecule one changed by 120° (↑↑↑); for model d) all torsions of both molecules changed by 120° (↑↑↑↑↑↑); and for model e) all torsions of molecule one changed by 120° and all torsions of molecule two by -120° (↑↑↑↓↓↓). For those the Rietveld profiles were calculated and double-quantum build-up curves were simulated.

Computational Methods: Before the *ab initio* structure solution of compound **1**, the molecule was geometry optimised by DFT methods using the module DMol3 of the program package Accelrys MS Modeling (version 5.0).[46] A double zeta plus polarisation basis set with the GGA functional PW91 was applied.[52] The self-consistent field (SCF) energy convergence was set to 10^{-6} eV per atom.

Results and Discussion

To gain insight into the structure directing effect of fluorine substitution in the side groups of **2**, the crystal structure of **1** was solved by a combination of PXRD and solid-state NMR experiments. First, we deduce the content of the asymmetric unit from multinuclear 1D solid-state NMR experiments. With this information a structure model is obtained from PXRD data based on real space methods and quantum chemical calculations. Finally, the structural disorder of the side groups is probed by double-quantum dipolar recoupling experiments.

Symmetry considerations using solid-state NMR: Figure 1 and 2 depict the high-resolution 1D spectra of ^{1}H, ^{19}F, ^{13}C and ^{15}N. The ^{1}H spectrum (Figure 1a) exhibits three signal groups. Group 1 is located between δ = 9 ppm and 8.5 ppm, group 2 between δ = 8.5 ppm and 5 ppm and group 3 below δ = 4 ppm. The intensity ratio for the groups 1:2:3 is 1.0:1.0:6.1. The shift

of group 1 is characteristic for the NH protons 4 (compare Scheme 1 for labeling) participating in weak hydrogen bonds,[53] the shift of group 2 for aromatic the CH groups 6 and group 3 exhibits a typical shift region for the methyl groups 1. Furthermore, the intensity ratio fits the ratio expected from the molecular structure (compare Scheme 1, 3 NH : 3 CH : 18 CH_3 protons). Since the aromatic CH signals exhibit a splitting into at least four different resonances, more than one molecule must be contained in the asymmetric unit.

The ^{19}F spectrum (Figure 1b) shows five well separated signal groups. High resolution 2D double-quantum single-quantum (DQSQ) correlation experiments (see Figure 3a and b) reveal that the most intense signal in the middle corresponds to two coinciding peaks (peaks 3 and 4 of Figure 1b). The deconvolution of the spectrum reveals an additional signal on the right side of the signal group (peak 7 of Figure 1b). Since it does not show any couplings to the remaining peaks in the 2D DQSQ correlation experiment (Figure 3a), it is identified as impurity and can be neglected for the following discussion. The remaining peaks 1 – 6 exhibit an intensity ratio of 1.0:1.4:1.4:1.0:1.0:0.9 which implies that the asymmetric unit must contain at least two molecules. The relatively high intensities of the peaks 2 and 3 are probably due to uncertainties in background correction.

In the $^{1}H^{15}N$ CP spectrum (Figure 1c), a signal group around δ = -258 ppm is observed, which is typical for the amide units 4. It exhibits at least four distinct resonances, which support the assumption of two or more independent molecules contained in the asymmetric unit.

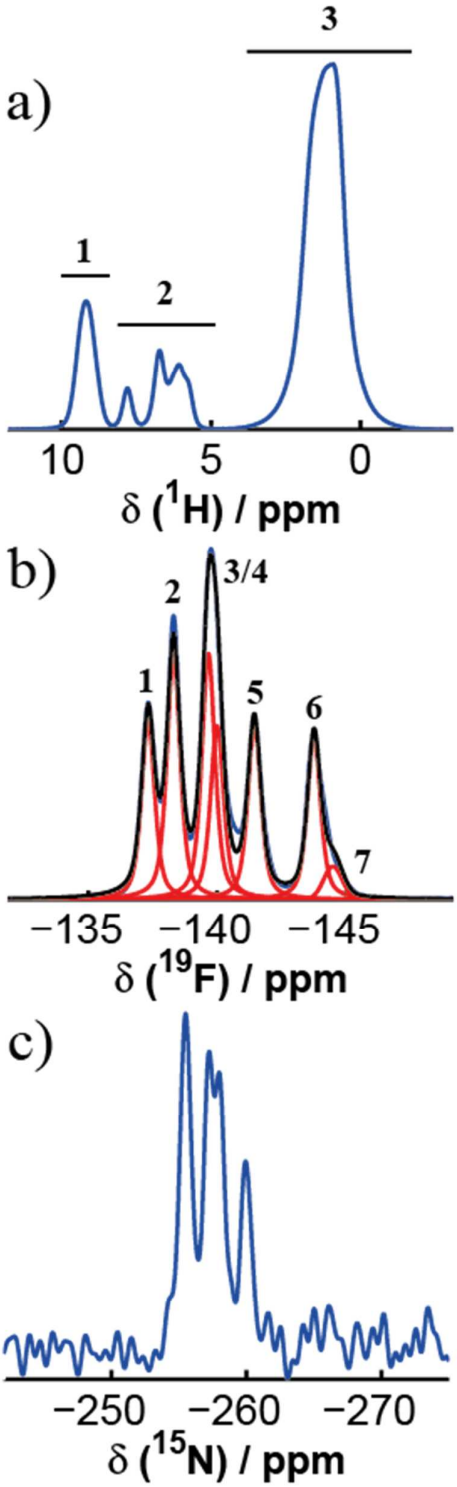

Figure 1. Solid-state NMR spectra of **1**. a) ^{1}H MAS spectrum obtained with single pulse excitation. The intensity ratio for the spectral regions 1-3 are 1:1.0:6.1; b) ^{19}F spectrum obtained with single-pulse excitation and deconvolution into peaks 1-7. The intensity ratio for peaks 1-6 are 1.4:1.4:1:1.0:0.9. Peak 7 is assigned to an impurity (see text and Figure 3); c) ^{15}N spectrum obtained by ^{1}H^{15}N cross polarization.

In order to assign the ^{13}C resonances, $^{1}H^{13}C$ and $^{19}F^{13}C$ CP experiments are analysed (Figure 2). Hereby, the contact time was chosen in order to highlight the strongest $^{1}H^{13}C$ and $^{19}F^{13}C$ connectivities (for details see experimental section). First, in the $^{1}H^{13}C$ CP six signal groups appear (Figure 2a). Group 1 at δ = 172 ppm is characteristic for the carbonyl groups 3 and group 6 around δ = 25 ppm is typical for the methyl groups 1. Due to their spatial proximity to fluorine atoms, they are also observed in the $^{19}F^{13}C$ CP (see Figure 2b). Group 2 of the $^{1}H^{13}C$ CP is characteristic for the quaternary aromatic carbon atoms 2 and group 3 and 4 for the aromatic CH units 6. Since their distance to the fluorine atoms in the molecular structure is long, they do not appear in the $^{19}F^{13}C$ CP. The remaining group 5 must, therefore, belong to the quaternary carbons 2 which are directly attached to the ^{19}F spins. This is supported by the $^{19}F^{13}C$ CP, in which group 5 exhibits quite intense signals. Since groups 3 and 4 together show at least 5 distinct resonances for the aromatic CH groups, the ^{13}C signals also indicate that two molecules are contained in the asymmetric unit.

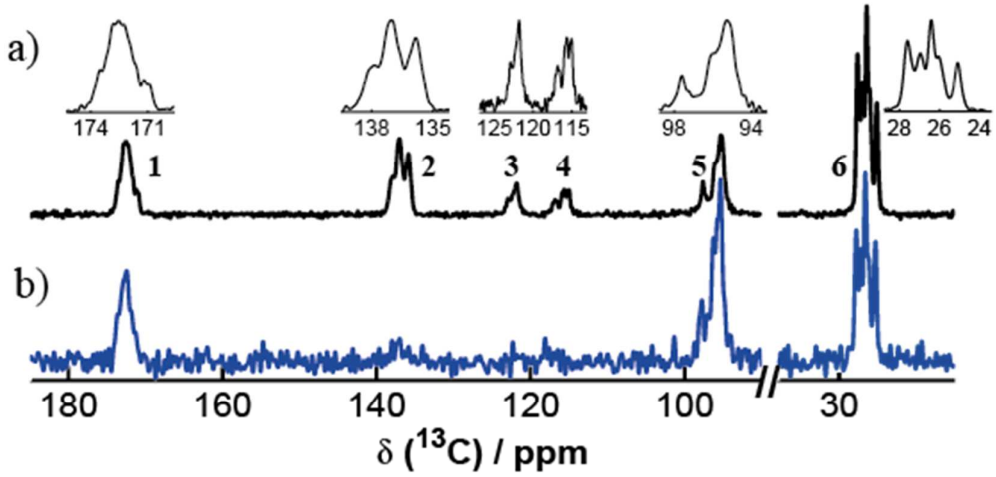

Figure 2. ^{13}C solid-state NMR spectra of compound **1**. a) $^{1}H^{13}C$ CP experiments with close-ups of the six groups; b) Same shift region of the $^{19}F^{13}C$ CP experiment. The groups are labelled by 1-6 as depicted.

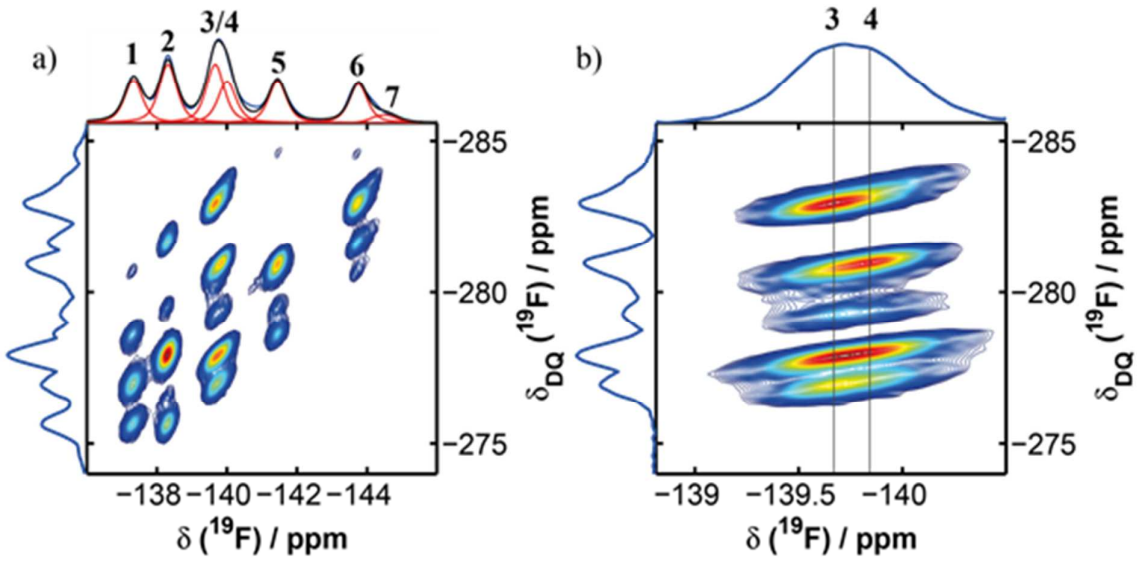

Figure 3. a) $^{19}F^{19}F$ double-quantum single-quantum correlation spectrum of **1**. On the top the deconvolution of the onepulse experiment (compare Figure 1b) is depicted. Only the area containing signals is depicted; b) Close-up of the area around the peak 3 and 4 of a), where the lines mark the shifts of the two distinct signals. Signal 7 exhibits no correlations.

In conclusion, most resonances for the individual chemical building units are split in several signals. For the aromatic CH groups, at least four resonances are visible in the ^{1}H and five resonances in the ^{13}C spectrum, respectively, six signals with roughly equal intensities appear in the ^{19}F direct excitation experiment and the ^{15}N spectrum exhibits at least four resonances for the NH groups. Therefore, the asymmetric unit has to contain at least two molecules. Moreover, the ^{1}H chemical shift of the NH group is indicative for moderate hydrogen bonds and only one peak is present for the NH protons. Thus, all of them are expected to participate in a homogeneous hydrogen bond network without significant differences in the strength of the hydrogen bonds.[5,13]

Crystal structure solution of 1,3, 5-tris (2-fluoro-2-methylpropionylamino) benzene from PXRD and solid-state NMR spectroscopy: Indexing of the powder pattern leads to a monoclinic metric. The subsequent refinement in *P*2 using the Pawley algorithm[54] results in lattice constants of a = 11.916 Å, b = 15.433 Å, c = 10.580 Å and β = 95.011° and a unit cell volume of 1924 Å^3. Analysing the integral extinction conditions leads to 8 possible space groups (*P*2, *P*2$_1$, *Pc*, *Pm*, *P*2/*m*, *P*2$_1$/*m*, *P*2/*c*, *P*2$_1$/c). Assuming that all non-hydrogen atoms within this compound (C, F, N, O) possess a volume of approximately 18 Å^3, the molecular

volume can be estimated to roughly 490 Å^3. Compared to the unit cell volume of 1924 Å^3, this size restriction allows maximum four molecules within the unit cell. Additionally, the ^{1}H, ^{13}C, ^{15}N and ^{19}F solid-state NMR spectra indicate that the asymmetric unit consist of at least two BTA molecules. Since the molecule itself does not possess a mirror plane or an intrinsic C2 symmetry, a location of all atoms on special positions within the unit cell is very unlikely. Therefore, the multiplicity of the general position must be 2 and only *P*2, *P*2$_1$, *Pm* and *Pc* remain as possible space groups. A more detailed analysis of the experimental powder pattern reveals that odd reflections of the 0k0 series are systematically absent, which strongly favours the space group *P*2$_1$.

Within space group *P*2$_1$ an *ab initio* structure solution with real space methods was performed based on a combination of a close-contact penalty and wRp as cost function. The DFT geometry optimized molecule was set twice in the unit cell and treated independently as rigid body with three rotational and three translational degrees of freedom for each molecule during the solution step. Additionally, the two most important, structure directing torsion angles (see Scheme 1, left) were varied during the solution step. The wRp value after the solution accounted for 14.66 %, a full Rietveld refinement finally led to a wRp value of 5.5 %. The resulting metric has unit cell constants of a = 11.886(4) Å, b = 15.394(5) Å, c = 10.553(4) Å and β = 95.011(2) ° and contains four molecules in the unit cell. The experimental powder data and the Rietveld profile are depicted in Figure 4.

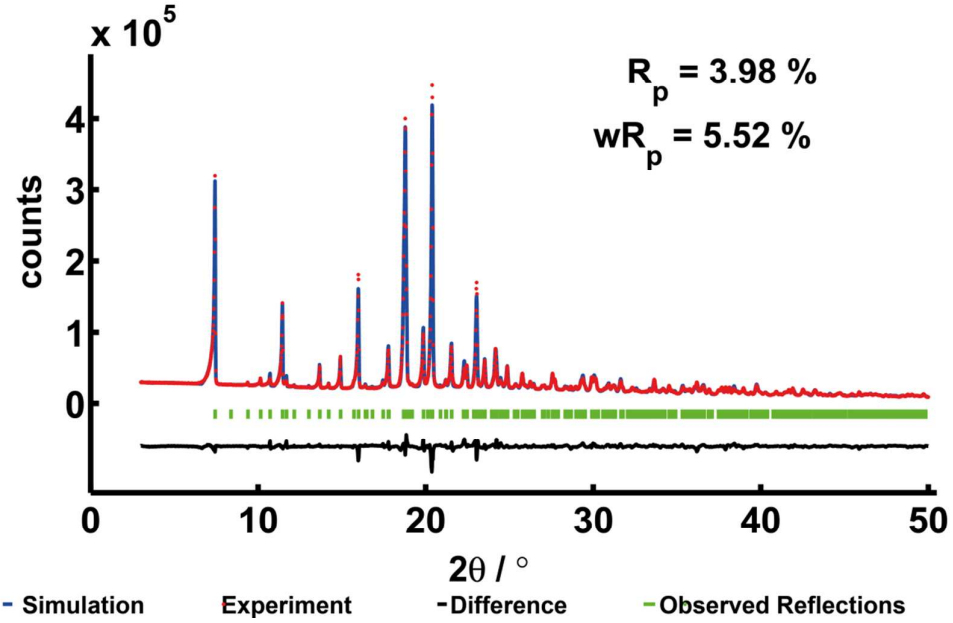

Figure 4. Rietveld profile plot of the PXRD pattern in space group *P*2$_1$ collected at room temperature in a 2Θ range of 2° - 50° using $Cu_{K\alpha 1}$ radiation. The difference plot is shifted by -0.6·10^{-5} counts.

Since the electron density gives rise to the scattering in X-ray diffraction, the difference between atoms or groups with similar or equal electron densities are blurred. The methyl groups and fluorine atoms both possess 9 electrons which makes them hard to distinguish by PXRD experiments. This indicates that their positions could be exchanged and even a random distribution might be possible.

To probe this hypothesis, the methyl groups and fluorine atoms of one or both molecules in the asymmetric unit were rotated in different ways by changing the $N_HC_OC_QF$ torsion angles (see Scheme 1, left) and subsequent Rietveld refinement as described in the experimental section. From the resulting structure models, three were selected in addition to the original structure solution a) in order to probe the effect of methyl-fluorine exchange on the calculated Rietveld patterns. In model b), one $N_HC_OC_QF$ torsion of the first molecule of the asymmetric unit was changed by approximately 120°, which will be symbolically depicted by ↑. In model c), all $N_HC_OC_QF$ torsions of the first molecule changed by approximately 120° (↑↑↑) and in model d) all $N_HC_OC_QF$ torsions of both molecules changed by approximately 120° (↑↑↑↑↑↑). Finally, for model e), all $N_HC_OC_QF$ torsions of the first molecule changed by approximately 120° and all $N_HC_OC_QF$ torsions of the second molecule by -120° (↑↑↑↓↓↓). The Rietveld profiles calculated from those models are contained in Figure S2 and S3 in the ESI†. Figure 5 (left) depicts the difference plots between the observed powder diffractogram and calculated Rietveld profiles.

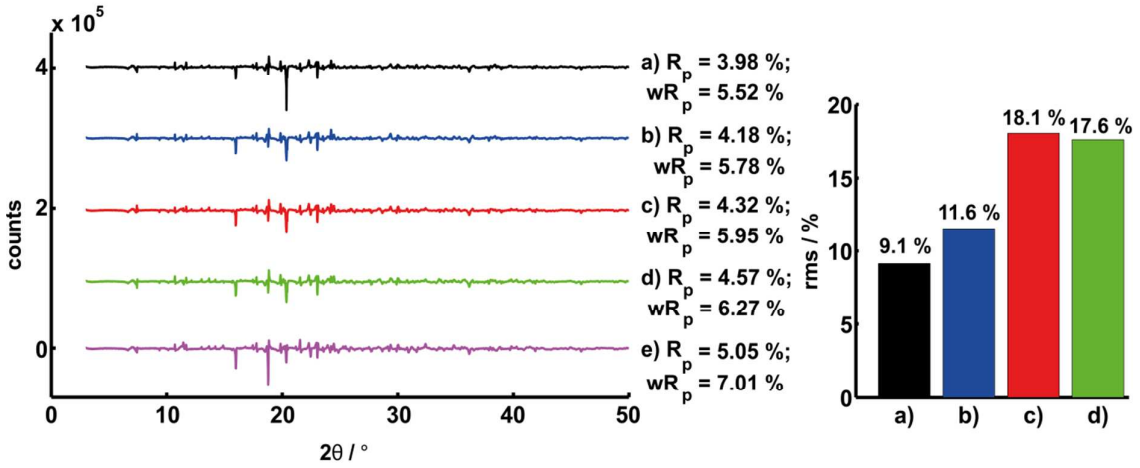

Figure 5. Left: Difference plots between the experimental PXRD data and calculated Rietveld profiles for the different structure models a)-e) after refinement. The difference plots are shifted by $4 \cdot 10^{-5}$ counts for model a), by $3 \cdot 10^{-5}$ counts for model b), $2 \cdot 10^{-5}$ counts for model c) and 10^{-5} counts for model d). Right: rms values of the deviations between the $^{19}F^{19}F$-DQ

build-up simulations for the different structure models a)-e) and the experimental data. For a detailed explanation of the models see text and experimental section.

The significantly higher Rp and wRp values of model e) imply that the resulting structure is unlikely with larger deviations in the packing compared to the other models. For b)-d), however, the difference plots are quite similar and the wRp values differ by 0.75 % at most, which implies similar electron density distributions. In conclusion, the $N_H C_O C_Q F$ torsions cannot be determined with reasonable accuracy by PXRD.

Here, solid-state NMR can assist by probing distance relations through quantitative symmetry-based DQ dipolar recoupling experiments. The $^{19}F^{19}F$ homonuclear dipolar interaction was selectively recoupled by applying a $SR14_4^5$ sequence which leads to an excitation of $^{19}F^{19}F$ double-quantum coherences. Since the dipolar interaction constant depends inversely on the third power of the internuclear distance, the recoupling efficiency encodes the structural environment of each spin. Moreover, the inverse cubic relation implies that already small structural changes may lead to high deviations in dipolar couplings. Here, we used symmetric build-up curves which were simulated for structure models a) - d). For every model, a 9-spin system was created for each ^{19}F of the asymmetric unit by taking all spins into account within a sphere with a diameter of 13.4 Å at least (see ESI† Figure S4). The relevant rms values are depicted in Figure 5 (right).

The original structure solution a) shows the best rms value of 9.1 %, whereas for the remaining models the rms values are at 11.6 % or above. Figure 6 depicts the experimental build-up curves for the six ^{19}F resonances with the simulated curves for the four structure models a)-d).

The simulations are scaled by a unique constant factor for each model in order to compensate residual dipolar proton couplings. This leaves the position of the first maximum and minimum and, therefore, the structural information unaffected. In all cases, the experimental curves show a fast build-up with maxima around an excitation time of $\tau_{excitation}$ = 1 ms. For the original structure model a) the curves fit very well for peak 3 - 6. For peak 1 and 2 the scaled simulations reach higher double-quantum efficiencies as the experimental curves. These two peaks reach their maximum at slightly longer excitation times compared to signals 3-6 which implies weaker homonuclear $^{19}F^{19}F$ interactions with the consequence of a stronger influence of residual dipolar proton couplings.

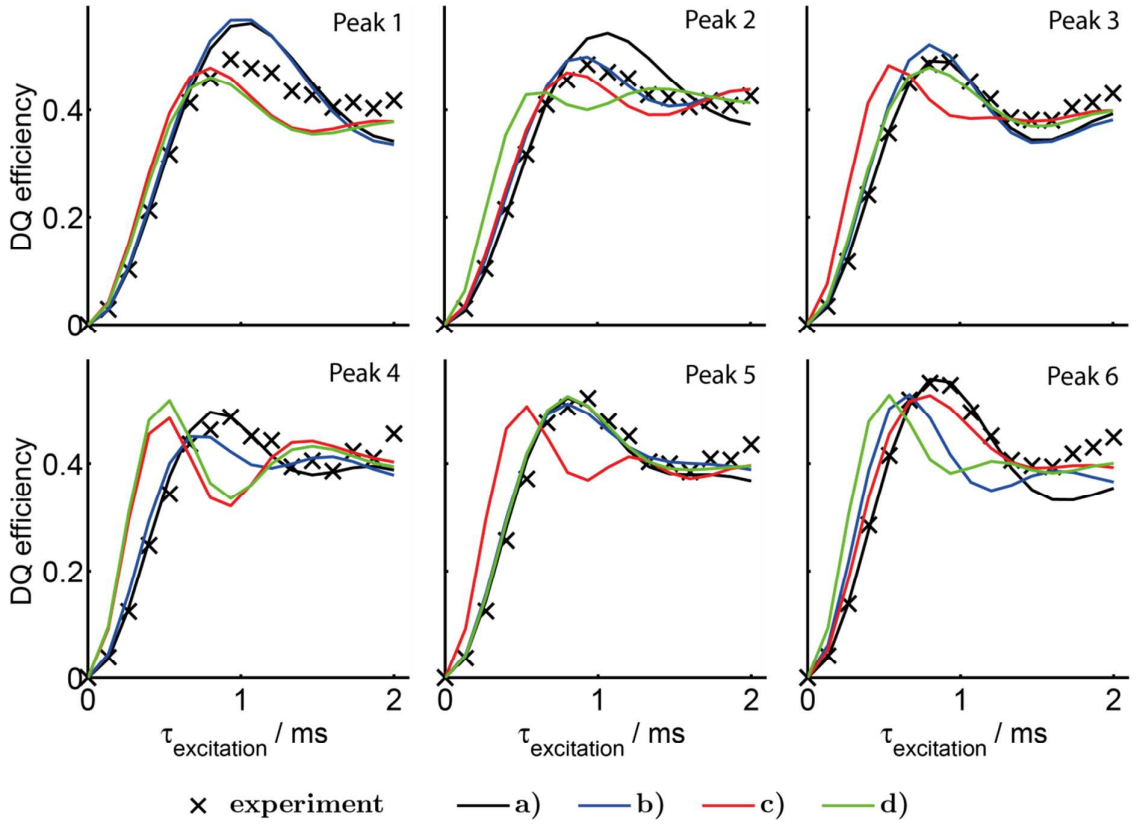

Figure 6. Experimental and simulated $^{19}F^{19}F$ build-up curves. The assignment of simulated to experimental curves was chosen according to the smallest rms values. The experimental curves are labeled with respect to the corresponding peaks in the ^{19}F spectrum (see Figure 1b) and the simulations a) - d) according to the structure models (see Figure 5 and text). Each set of simulations was scaled by a constant factor of 0.75 in the case of a) and c) and 0.79 for the case of b) and d), respectively.

In contrast to model a), the remaining structure models b) - d) show more pronounced deviations compared to the experiment. In all cases, at least two build-up curves exist which exhibit a faster rise, e.g. as in the case of the models c) and d) for peak 4. This implies shorter $^{19}F^{19}F$ distances since the total number of ^{19}F is the same for all simulations. In fact, the shortest $^{19}F^{19}F$ distances for the models a) - d) are 3.9 Å, 3.8 Å, 3.4 Å and 3.4 Å, respectively, and hence the corresponding coupling constants are -1794 Hz, -1940 Hz, -2708 Hz. Thus, the sensitivity of this experiment towards structural details is high, complementing the information obtained from the PXRD experiment. The lowest wRp value of 5.52 % together with the superior rms value of 9.1 % strongly favours structure model a).

Crystal structure of 1, 3, 5-tris (2-fluoro-2-methylpropionylamino) benzene: The molecular structures of the two independent molecules (**1a** and **1b**) after the Rietveld refinement are depicted in Figure 7 and the most important intramolecular distances and angles are listed in Table 2.

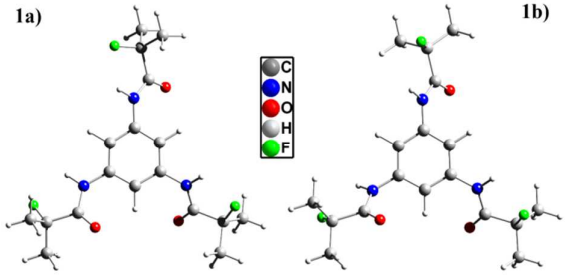

Figure 7. Molecular structures of the two independent molecules of the asymmetric unit of 1,3,5-tris(2-fluoro-2-methylpropionylamino)benzene **1** as derived from the PXRD experiment.

Table 2. Intramolecular distances in angstrom and angles in degree derived from PXRD with restrictions based on the COMPASS forcefield used for the first Rietveld refinement step. The distances marked by * use the positions of the protons determined through DFT geometry optimisation of a single molecule.

	Molecule 1	**Molecule 2**
d(C = O)	1.214	1.211 - 1.213
d(C_{Ar} - N)	1.390 - 1.396	1.397 - 1.398
d(C_O - N)	1.368 - 1.369	1.368 - 1.373
d(C_{Ar} - C_{Ar})	1.381 - 1.387	1.382 - 1.386
d(C_q - C_{Me})	1.525 - 1.529	1.526 - 1.533
d(C - F)	1.390	1.388 - 1.391
d(NH---F)	2.121 - 2.171*	2.239 - 2.268*
∡(NH---F)	107.0 - 109.2	103.9 - 105.9
∡(HNCO)	173.2 - 177.1	176.5 - 177.0
∡($C_{Ar}C_{Ar}$NH)	-152.9, 40.7, 40.8	-124.5, 36.5, 57.0
∡($N_HC_OC_q$F)	6.86 - 25.04	26.15 - 31.81
∡(OC_OC_qF)	156.0 - 175.1	150.7 - 158.4

Interestingly, both molecules exhibit weak NH---F contacts with proton-fluorine distances between 2.1 Å - 2.3 Å. Hereby, the proton positions were determined through DFT geometry optimisation of a single molecule and retained during Rietveld refinement due to the energy constraint by the applied forcefield. Moreover, both molecules exhibit a high topological similarity although they are not related through symmetry operations. For both molecules, two of the three carbonyl groups point up and one points downwards with respect to the benzene plane leading to an intrinsically frustrated molecular system. The corresponding $C_{Ar}C_{Ar}NH$ torsion angles are 40.65°, 40.82° and -152.85° for molecule 1 and 36.49°, 57.0° and -124.53° for molecule 2, respectively. The NHCO torsion angles representing the amide groups show values between 173° and 177° which are typical values for partial double bonds. Besides, the torsions including the fluorine atoms within the side groups ($N_HC_OC_qF$) are also distinguishable with values between roughly 7° - 32°. These locally different fluorine environments are in agreement with the six distinct resonances observed in the 1D ^{19}F solid-state NMR (see Figure 1b).

The crystal structure of **1** can be described as hydrogen bond mediated layer-like structure including a molecular zigzag motif due to the 2_1 screw axis along the *b*-axis of the unit cell. The two independent molecules of the asymmetric unit (see Figure 8, black colour) are incorporated into one strand along the crystals' *c*-axis *via* four moderate NH---OC H-bonds with lengths of 2.03 Å and 2.22 Å (corresponding to NH---OC lengths of 2.93 Å and 3.20 Å, see Figure 8, dashed pink lines) and NH---O angles located in the range of 146.9° and 162.1°, respectively.

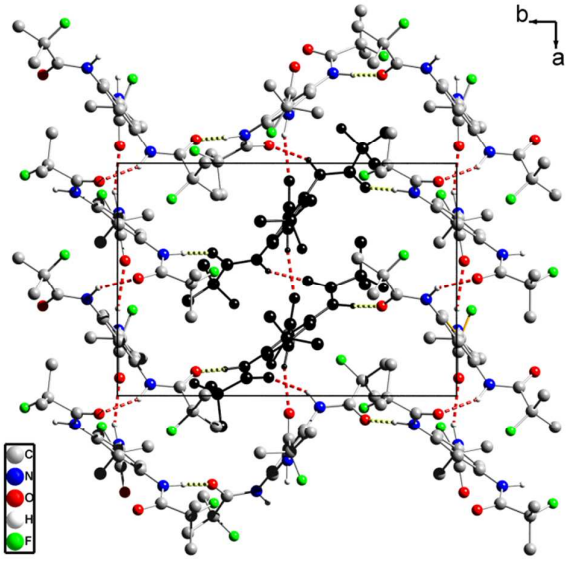

Figure 8. Hydrogen bond pattern of compound **1**. The two independent molecules of the asymmetric unit (black colour) are connected to strands through four H-bonds (dashed red

lines). The strands are further connected by two lateral hydrogen bonds along the *b*-axis of the crystal (dashed green lines) leading to a two-dimensional layer-like hydrogen bond pattern. All protons except the amide ones as well as the $C_q(CH_3)_2F$ groups are omitted for clarity.

The distances between the aromatic cores of the molecules within one strand accounts for 5.15 Å up to 5.64 Å ruling out the existence of any π-π-interactions as observed in other BTA related systems.[9,11,13] The aromatic benzene rings thereby show a tilt angle of roughly 16° towards each other. These one-dimensional strands are connected with a neighbouring strand which arises from the translation through the 2_1 screw axis along the monoclinic axis. Here, two lateral medium strong NH---OC hydrogen bonds with N---O lengths of 2.89 Å and 2.94 Å are observed (see Figure 8, dashed green lines), the related NH---O angles account for 157.9° and 160.7°, respectively. Interestingly, none of the six independent fluorine atoms participate in intermolecular hydrogen bonds.

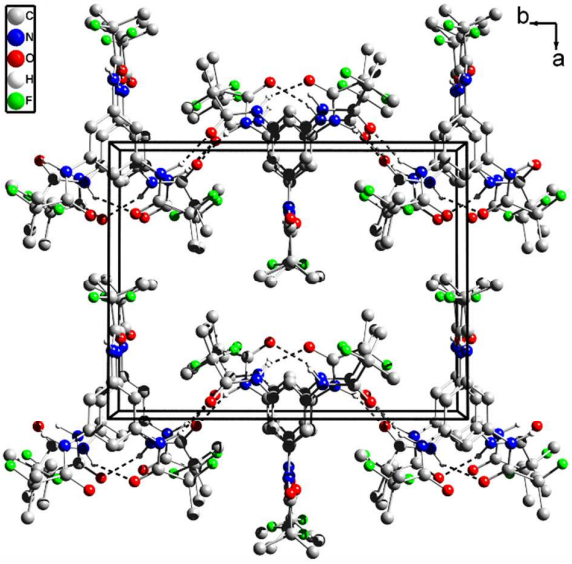

Figure 9. Perspective view over two unit cells along the *c*-axis demonstrating the layer-like character of the structure. All protons except those of the amide group are removed to retain clarity. Between neighbouring layers only van-der-Waals interactions are possible.

Thus, a two-dimensional layer-like structure within the b-c-plane of the crystal is observed and, due to the translational symmetry, a second layer arises along the crystalline *a*-axis (see Figure 9). Since between neighbouring layers only van-der-Waals interactions are relevant, the interaction pattern in the structure is highly anisotropic.

Conclusion

We used a concerted approach of multidimensional and multinuclear solid-state NMR spectroscopy, *ab initio* real space PXRD methods and computer simulations to solve the structure of 1,3,5-tris(2-fluoro-2-methylpropionylamino)benzene. It can be described by a lamellar arrangement of molecules. Within each layer, strong to moderate, two-dimensional hydrogen bond patterns along be *b*- and *c*-axes with N---O distances ranging from 2.9 Å up to 3.2 Å are formed. The molecules are stacked along the *c*-axis, where neighbouring benzene rings exhibit a non-coplanar arrangement and distances ranging from 5.15 Å up to 5.64 Å which prevent π-π-interactions. In each molecule the amide bonds are tilted with respect to the benzene rings in a way that only two out of three carbonyl groups point into the same direction. Surprisingly, the fluorine atoms contribute only to weak intramolecular NH---F contacts but not to the intermolecular hydrogen bond network. Since between neighbouring layers only van-der-Waals interactions are possible, the interaction pattern is highly anisotropic and one might expect a fast two-dimensional crystal growth along the crystals *b*- and *c*-axes, rendering this BTA an interesting candidate for formation of two-dimensional structures *via* self-assembly.

In the analogous BTA 1,3,5-tris(2,2-dimethylpropionylamino)benzene **2**, where just the fluorine atoms of **1** are replaced by methyl groups, the molecules are arranged in columnar stacks. The latter are stabilized by moderate helical hydrogen bonds in combination with π-π-interactions.[13] All amide bonds of the molecules within one column are also tilted with respect to the benzene core and point into the same direction so that a macrodipole is formed. Due to an antiparallel arrangement of those macrodipoles in neighbouring columns of the pseudo-hexagonal rod packing, the net dipole moment is cancelled. This allows for fast one-dimensional growth through cooperative effects in the hydrogen bond network.[12,13,55]

In spite of the similarities in the molecular structures of **1** and **2**, in particular with respect to the sterical demand of the side groups, completely different crystal structures are formed. Since fluorine does not participate in the hydrogen bond network, we assume that the different molecular polarity is responsible for this effect. This illustrates the versatility of BTAs and the easy accessibility of new packing motifs by small chemical modifications.

Acknowledgements

The authors want to thank the DFG (SFB 840, Project B4) for funding this work and Dr. Wolfgang Milius for the fruitful discussions with respect to crystallographic issues. C.Z. thanks the Elitenetzwerk Bayern (ENB) for additional support. Martin Hufnagel is gratefully acknowledged for performing MALDI-TOF MS measurements.

References

1 a) J.-M. Lehn, *Angewandte Chemie*, 1988, **100**, 91; b) L. Brunsveld, B. J. B. Folmer, E. W. Meijer and R. P. Sijbesma, *Chem. Rev.*, 2001, **101**, 4071.

2 J.-M. Lehn, *Angew. Chem. Int. Ed.*, 1990, **29**, 1304.

3 P. J. M. Stals, M. M. J. Smulders, R. Martín-Rapun, A. R. A. Palmans and E. W. Meijer, *Chem.-Eur. J.*, 2009, **15**, 2071.

4 P. J. M. Stals, J. C. Everts, R. de Brujin, I. A. W. Filot, M. M. J. Smulders, R. Martin-Rapun, E. A. Pidko, T. F. A. de Greef, A. R. A. Palmans and E. W. Meijer, *Chem.-Eur. J.*, 2010, **16**, 810.

5 M. Wegner, D. Dudenko, D. Sebastiani, A. R. A. Palmans, T. F. A. de Greef, R. Graf and H. W. Spiess, *Chem. Sci.*, 2011, **2**, 2040.

6 M. Schmidt, C. S. Zehe, R. Siegel, J. U. Heigl, C. Steinlein, H.-W. Schmidt and J. Senker, *CrystEngComm*, 2013, **15**, 8784.

7 K. Hanabusa, C. Koto, M. Kimura, H. Shirai and A. Kakehi, *Chem. Lett.*, 1997, **26**, 429.

8 S. Cantekin, T. F. A. de Greef and A. R. A. Palmans, *Chem. Soc. Rev.*, 2012, **41**, 6125.

9 M. P. Lightfoot, F. S. Mair, R. G. Pritchard and J. E. Warren, *Chem. Commun.*, 1999, 1945.

10 a) L. Brunsveld, A. P. H. J. Schenning, M. A. C. Broeren, H. M. Janssen, J. A. J. M. Vekemans and E. W. Meijer, *Chem. Lett.*, 2000, **99**, 292; b) D. Kluge, F. Abraham, S. Schmidt, H.-W. Schmidt and A. Fery, *Langmuir*, 2010, **26**, 3020; c) D. Kluge, J. C. Singer, J. W. Neubauer, F. Abraham, H.-W. Schmidt and A. Fery, *Small*, 2012, **8**, 2563.

11 M. Kristiansen, P. Smith, H. Chanzy, C. Baerlocher, V. Gramlich, L. McCusk, T. Weber, P. Pattison, M. Blomenhofer and H.-W. Schmidt, *Cryst. Growth Des.*, 2009, **9**, 2556.

12 R. Q. Albuquerque, A. Timme, R. Kress, J. Senker and H.-W. Schmidt, *Chem.-Eur. J.*, 2013, **19**, 1647.

13 M. Schmidt, J. Wittmann, R. Kress, D. Schneider, S. Steuernagel, H.-W. Schmidt and J. Senker, *Cryst. Growth Des.*, 2012, **12**, 2543.

14 a) Y. Yasuda, E. Iishi, H. Inada and Y. Shirota, *Chem. Lett.*, 1996, **25**, 575; b) J. J. van Gorp, J. A. J. M. Vekemans and E. W. Meijer, *J. Am. Chem. Soc.*, 2002, **124**, 14759.

15 a) N. Shi, H. Dong, G. Yin, Z. Xu and S. Li, *Adv. Funct. Mater.*, 2007, **17**, 1837; b) A. Bernet, R. Q. Albuquerque, M. Behr, S. T. Hoffmann and H.-W. Schmidt, *Soft Matter*, 2012, **8**, 66.

16 Y. Matsunaga, N. Miyajima, Y. Nakayasu, S. Sakai and M. Yonenaga, *Bull. Chem. Soc. Jpn.*, 1988, **61**, 207.

17 P. Besenius, J. L. M. Heynens, R. Straathof, M. M. L. Nieuwenhuizen, P. H. H. Bomans, E. Terreno, S. Aime, G. J. Strijkers, K. Nicolay and E. W. Meijer, *Contrast Media Mol. Imaging*, 2012, **7**, 356.

18 M. Gelinsky, R. Vogler and H. Vahrenkamp, *Inorg. Chem.*, 2002, **41**, 2560.

19 a) M. Blomenhofer, S. Ganzleben, D. Hanft, H.-W. Schmidt, M. Kristiansen, P. Smith, K. Stoll, D. Mäder and K. Hoffmann, *Macromolecules*, 2005, **38**, 3688; b) P. M. Kristiansen, A. Gress, P. Smith, D. Hanft and H.-W. Schmidt, *Polymer*, 2006, **47**, 249; c) F. Abraham, S. Ganzleben, D. Hanft, P. Smith and H.-W. Schmidt, *Macromol. Chem. Phys.*, 2010, **211**, 171.

20 F. Richter and H.-W. Schmidt, *Macromol. Mater. Eng.*, 2013, **298**, 190.

21 J. Wang, Q. Dou, X. Chen and L. Di, *J. Polym. Sci. Pol. Phys.*, 2008, **46**, 1067.

22 F. Abraham and H.-W. Schmidt, *Polymer*, 2010, **51**, 913.

23 a) H. Nakajima, M. Takahashi and Y. Kimura, *Macromol. Mater. Eng.*, 2010, **295**, 460; b) H. Bai, W. Zhang, H. Deng, Q. Zhang and Q. Fu, *Macromolecules*, 2011, **44**, 1233; c) P. Song, Z. Wei, J. Liang, G. Chen and W. Zhang, *Polym. Eng. Sci.*, 2012, **52**, 1058.

24 J. Senker, L. Seyfarth and J. Voll, *Solid State Sci.*, 2004, **6**, 1039.

25 L. Seyfarth, J. Sehnert, N. El-Gamel, W. Milius, E. Kroke, J. Breu and J. Senker, *J. Mol. Struct.*, 2008, **889**, 217.

26 J. C. Facelli and A. M. Orendt, Magnetic Shielding and Chemical Shifts: Basics, in *eMagRes*, 2007.

27 R. E. Wasylishen, Dipolar and Indirect Coupling: Basics, in *eMagRes*, 2007.

28 P. P. Man, Quadrupolar Interactions, in *eMagRes*, 2007.

29 a) M. Duer, *Introduction to solid-state NMR spectroscopy*, Blackwell, Oxford, U.K., 2004; b) R. K. Harris, R. E. Wasylishen and M. J. Duer, *NMR Crystallography*, Wiley, Chichester, U.K., 2nd edn., 2009.

30 a) F. Taulelle, *Solid State Sci*, 2004, **6**, 1053; b) F. W. Karau, L. Seyfarth, O. Oeckler, J. Senker, K. Landskron and W. Schnick, *Chem. Eur. J.*, 2007, **13**, 6841.

31 a) J. Senker, J. Sehnert and S. Correll, *J. Am. Chem. Soc.*, 2005, **127**, 337; b) J. Sehnert and J. Senker, *Chem. Eur. J.*, 2007, **13**, 6339-6350.

32 a) M. Schmidt, J. Wittmann, R. Kress, H.-W. Schmidt and J. Senker, *Chem. Commun.*, 2013, **49**, 267; b) E. Wirnhier, M. Döblinger, D. Gunzelmann, J. Senker, B. V. Lotsch and W. Schnick, *Chem. Eur. J.*, 2011, **17**, 3213; c) D. Hirsemann, T. K.-J. Köster, J. Wack, L. van Wüllen, J. Breu and J. Senker, *Chem. Mater.*, 2011, **23**, 3152.

33 L. Seyfarth, J. Seyfarth, B. Lotsch, W. Schnick and J. Senker, *Phys. Chem. Chem. Phys.*, 2010, **12**, 2227.

34 L. Seyfarth and J. Senker, *Phys. Chem. Chem. Phys.*, 2009, **11**, 3522.

35 a) J. Senker and J. Lüdecke, *Z. Naturforsch.*, 2001, **56b**, 1089; b) E. Salager, R. S. Stein, C. J. Pickard, B. Elena and L. Emsley, *Phys. Chem. Chem. Phys.*, 2009, **11**, 2610; c) D. V. Dudenko, P. A. Williams, C. E. Hughes, O. N. Antzutkin, S. P. Velaga, S. P. Brown and K. D. M. Harris, *The Journal of Physical Chemistry C*, 2013, **117**, 12258; d) M. R. Chierotti, R. Gobetto, C. Nervi, A. Bacchi, P. Pelagatti, V. Colombo and A. Sironi, *Inorganic Chemistry*, 2014, **53**, 139.

36 C. Martineau, J. Senker and F. Taulelle, NMR Crystallography, in *Annu. Rep. NMR Spectros.*, vol. 82, pp. 1.

37 C. A. Jimenez, J. B. Belmar, L. Ortiz, P. Hidalgo, O. Fabelo, J. Pasan and C. Ruiz-Perez, *Cryst. Growth Des.*, 2009, **9**, 4987.

38 X. Hou, M. Schober and Q. Chu, *Cryst. Growth Des.*, 2012, **12**, 5159.

39 a) Y. Matsunaga, Y. Nakayasu, S. Sakai and M. Yonenaga, *Mol. Cryst. Liq. Cryst.*, 1986, **141**, 327; b) A. Timme, R. Kress, R. Q. Albuquerque and H.-W. Schmidt, *Chem.-Eur. J.*, 2012, **18**, 8329.

40 M. H. Levitt, Symmetry-Based Pulse Sequences in Magic-Angle Spinning Solid-State NMR, in *eMagRes*, 2007.

41 A. Detken, E. H. Hardy, M. Ernst and B. H. Meier, *Chem. Phys. Lett.*, 2002, **356**, 298.

42 M. Bak, J. T. Rasmussen and N. C. Nielsen, *J. Magn. Reson.*, 2000, **147**, 296.

43 P. E. Kristiansen, M. Carravetta, J. D. van Beek, W. C. Lai and M. H. Levitt, *J. Chem. Phys.*, 2006, **124**, 234510.

44 Y. K. Lee, N. D. Kurur, M. Helmle, O. G. Johannessen, N. C. Nielsen and M. H. Levitt, *Chem. Phys. Lett.*, 1995, **242**, 304.

45 The MathWorks, Inc., *MATLAB 2014a*, Natick, Massachusetts, United States, 2014.

46 Accelrys Inc., *MS Modeling v5.0.0.0*, San Diego, California, United States, 2009.

47 M. W. Deem and J. M. Newsam, *Nature*, 1989, **342**, 260.

48 W. A. Dollase, *J. Appl. Cryst.*, 1986, **19**, 267.

49 a) H. M. Rietveld, *J. Appl. Cryst.*, 1969, **2**, 65; b) H. Toraya and F. Marumo, *Mineral J*, 1981, **10**, 211.

50 H. Sun, *J. Phys. Chem. B*, 1998, **102**, 7338.

51 L. W. Finger, Cox D. E. and Jephcoat A. P., *J. Appl. Cryst.*, 1994, **27**, 892.

52 J. P. Perdew and Y. Wang, *Phys. Rev. B*, 1992, **45**, 13244.

53 M. R. Chierotti and R. Gobetto, *Chem. Commun.*, 2008, 1621.

54 G. S. Pawley, *J. Appl. Crystallogr.*, 1981, **14**, 357.

55 I. A. W. Filot, A. R. A. Palmans, P. A. J. Hilbers, R. A. van Santen, E. A. Pidko and T. F. A. de Greef, *J. Chem. Phys. Chem. B*, 2010, **114**, 13667.